JPE

Coordinative Control Strategy for Power Electronic Transformer Based Battery Energy Storage System

Yuwei Sun*, Jiaomin Liu*, Yonggang Li*, Chao Fu†, and Yi Wang*

*†State Key Laboratory of Alternate Electrical Power System with Renewable Energy Sources, North China Electric Power University, Baoding, China

Abstract

Power electronic transformer (PET) based on the cascaded H-bridge (CHB) and isolated bidirectional DC/DC converter (IBDC) is capable to accommodate large scale battery energy storage system (BESS) in the medium-voltage grid, named as power electronic transformer based battery energy storage system (PET-BESS). This paper investigates the PET-BESS and proposes a coordinative control strategy for it. In the proposed method, the CHB controls the power flow and battery state-of-charge (SOC) balancing, while the IBDC maintains the dc-link voltages with feedforward implementation of power reference and switch status of CHB. State-feedback and linear quadratic riccati (LQR) methods have been adopted in CHB to control the grid current, active and reactive power. A hybrid PWM modulating method is utilized to achieve SOC balancing, where battery SOC sorting is involved. The feedforward path of power reference and CHB switch status substantially reduces the dc-link voltage fluctuations under dynamic power variations. The effectiveness of the proposed control has been verified by both simulation and experimental results, not only the performance of the PET-BESS under bidirectional power flow has been improved, but also the battery SOC values have been adjusted to converge.

Key words: Battery energy storage, Coordinative control, LQR, Power electronic transformer, State-feedback, SOC balancing

I. INTRODUCTION

The increasing penetration of intermittent renewable energy resources, such as solar and wind generation, brings more challenges to the planning, operation and stability control of modern power system [1], [2]. By speedily storing and releasing electrical energy, battery energy storage system (BESS) gains more flexibility for the original "rigid" system. Thus, the installation of BESS, especially in grid scale, is indispensable to suppress the fluctuations of renewable energy sources and improve the power quality of renewable energy involved power systems [1], [3]-[5].

Normally the PV plant or wind farm with megawatt (MW) scale is integrated into the medium-voltage (MV) grid [6], and in China the voltage level is typically 10kV or 35kV, as shown in Fig. 1(a). For the BESS applied in this scenario, the power conversion system (PCS) with high power and MV ratings is crucial. The cascaded H-bridge (CHB) multilevel converter is a practical solution to achieve the MV level power conversion, since it can overcome the voltage limits of switching devices and generate multilevel ac waveforms with low total harmonic distortion (THD) [7]. Many researches have been conducted on the single-stage CHB converter based BESS. Dedicated active-power control of individual converter and state-of-charge (SOC) balancing control of the multiple battery units have been reported in [3] and [8] respectively.

However, the adoption of single-stage CHB in BESS directly integrates batteries on the dc buses of CHB, and it engages the problem of voltage-matching. Technically, the battery voltage experiences significant variation which is dependent on the SOC and internal impedance voltage drop of battery [9], [10]. This wide-range voltage variation on dc buses will cause distortion of the multilevel ac output. To ensure proper grid power transfer, the voltage of battery pack as well as the withstand voltage of the semiconductor switches have to be designed with certain rating margin [10]. Furthermore, the absence of galvanic isolation makes the safe operation of the BESS more vulnerable. The employment of intermediary isolated bidirectional DC/DC converter (IBDC)

can resolve the preceding issues. As an alternative to high-power DC/DC converter [11], the IBDC has received sufficient attention for high-power interface in smart grids, railway traction [12], etc., for its attractive features. It not only provides the functions of galvanic isolation and voltage conversion, but also has the advantages of high power density, bidirectional power transfer capability, ease of realizing soft-switching, modular and symmetric structure, etc. [13]. Actually, such a PCS using CHB and IBDC has become more prevalent in the modern power electronic transformer (PET) area, and is expected to play a key role in active management of distributed energy generations, energy storage systems, and loads [14]-[17]. The BESS based on the CHB-IBDC topology is therefore referred to as PET-BESS in this paper.

Previous studies on the CHB-IBDC type PET in [15]-[17] mainly considered the application of parallel connected IBDC. In these papers, the CHB not only controls the sinusoidal grid current, but also controls the summation of the dc-link voltages and voltage balance; while the IBDCs control the parallel output voltage and power balance of each cell. However, for the BESS, the IBDC outputs are connected to split battery units, with different control objectives. Besides the sinusoidal ac current and controllable active and reactive power on the grid side, the state of charge (SOC) balancing control of the split battery units should be guareented. Moreover, to enhance the dynamic feature under bidirectional BESS application, the coordinative control for fast balancing the transient power between CHB and IBDC is required. However, few literatures have addressed the above control issues overall. Literature [18] presentes the H bridge and IBDC based BESS, focusing on circuit optimal design rather than control strategies for multi-module cascade application. In [19], the coordinative control methods for CHB and half-bridge IBDC in the application of BESS has been reported, which applies the power feed-forward to the dc-link, but the battery SOC balancing is not taken into account.

This paper presents an overall coordinative control strategy for PET-BESS: Firstly, state-feedback and linear quadratic riccati (LQR) control methods are applied to optimize the CHB controller design. Secondly, a feed-forward path of the active power reference and switch status of CHB is added to the dc-link control for IBDC, and it can reduce the dc-link voltage fluctuation under the fluctuating bidirectional power. Thirdly, the battery SOC values are incorporated into the CHB's Hybrid PWM (HPWM) modulation process to achieve the SOC balancing of the submodule battery units.

The paper is organized as follows. Section 2 briefly introduces the configuration of PET-BESS and its overall control strategy. Then the controllers design are derived in Section 3. Section 4 illustrates the HPWM-based SOC balancing method for CHB rectifier. Finally, the proposed control methods are validated by simulation and experimental results, and then the conclusion is given in Section 6.

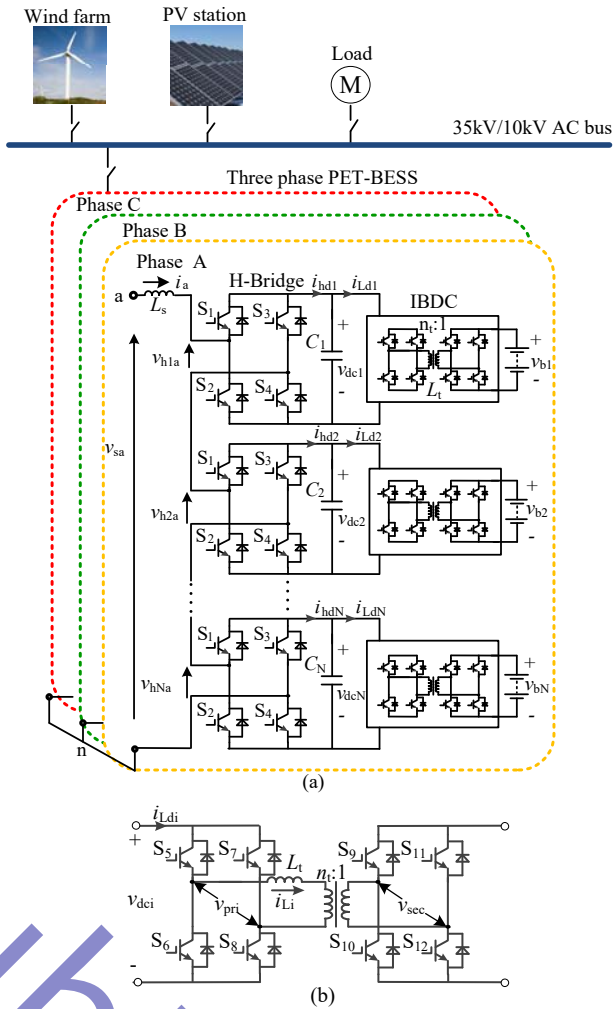

Fig. 1 Main circuit topology of PET-BESS. (a) Entire configuration for PET-BESS. (b) IBDC circuit composition.

II. System Configuration

A. Topology and Modeling of PET-BESS

Fig. 1(a) shows the configuration of PET-BESS and it consists of a CHB rectifier, N dc-link capacitors C_1~C_N, and N IBDC circuits per phase. The components in the leg of phase A are depicted in detail. v_{sa} and i_a are respectively the grid voltage and grid current; L_s is the input filter inductance; v_{h1a}~v_{hNa} are the ac output voltages of each H-bridge of CHB; v_{dc1}~v_{dcN} are the dc-link voltages; i_{hdi} and i_{Ldi} are the dc currents before and after dc-link capacitor respectively, and v_{b1}~v_{bN} are the battery-unit terminal voltages. The circuit composition of IBDC module is shown in Fig. 1(b), where n_t and L_t are the turn ratio and equivalent leakage inductance (on primary side) of HF transformer respectively; i_{Li} is the ac current flowing into the HF transformer, and v_{pri} and v_{sec} are the ac voltages of the primary side and secondary side of the transformer.

Since the objectives of the balancing control in this paper aim at the dc-link voltages and battery-SOC values among

submodules within one phase leg, the following assumptions are presented: 1) The three-phase gird voltages are balanced; 2) The three phase legs have equal average dc-link voltages and average battery SOC values; 3) The converter parameters of each module in each phase are identical.

In view of the same IBDC controllers and SOC balancing algorithm applied to all phases, the dc variables on the dc-link and battery side are not distinguished with subscripts a, b and c.

According to Fig. 1, assuming that the dc-link voltages are effectively controlled to the desired reference value v_{dcref}, i.e., $v_{\mathrm{dc1}}= v_{\mathrm{dc2}}=\ldots=v_{\mathrm{dcN}}=v_{\mathrm{dcref}}$, the relationship between the input quantities and the output quantities of CHB converter in phase A can be written as follows:

$$\begin{cases} v_{\mathrm{an}} = \sum_{i=1}^{N} v_{\mathrm{hia}} = \sum_{i=1}^{N} h_{\mathrm{ia}} \cdot v_{\mathrm{dci}} = v_{\mathrm{dcref}} \sum_{i=1}^{N} h_{\mathrm{ia}} \\ i_{\mathrm{hdi}} = h_{\mathrm{ia}} i_{\mathrm{a}} \quad , \quad (i = 1, 2 \cdots N) \end{cases} \tag{1}$$

where v_{an} is the synthesized multilevel ac voltage of CHB, and h_{ia} (i=1…N) represents the switching function of each H-bridge. When the two upper switches (S_1, S_3) or the bottom switches (S_2, S_4) conduct, h_{ia} equals zero; when the diagonal switches (S_1,S_4) or (S_2, S_3) conduct, h_{ia} equals 1 or -1, respectively. Then based on KVL, the grid current dynamic is expressed by the following equation:

$$L_{\mathrm{s}} \frac{\mathrm{d}\, i_{\mathrm{a}}}{\mathrm{d}\, t} + R_{\mathrm{s}} i_{\mathrm{a}} = v_{\mathrm{sa}} - v_{\mathrm{an}} = v_{\mathrm{sa}} - v_{\mathrm{dcref}} \sum_{i=1}^{N} h_{\mathrm{ia}} \tag{2}$$

The ac current dynamic equation of CHB in three-phase frame is expressed as:

$$\frac{\mathrm{d}}{\mathrm{d}\, t}[i]_{\mathrm{abc}} = -\frac{R_s}{L_s}[i]_{\mathrm{abc}} - \frac{v_{\mathrm{dcef}}}{L_s}[u]_{\mathrm{abc}} + \frac{1}{L_s}[v_{\mathrm{s}}]_{\mathrm{abc}} \tag{3}$$

where $[v_{\mathrm{s}}]_{\mathrm{abc}}$ denotes the grid phase-voltage vector $[v_{\mathrm{sa}}\ v_{\mathrm{sb}}\ v_{\mathrm{sc}}]^{\mathrm{T}}$; $[i]_{\mathrm{abc}}$ denotes the grid current vector $[i_{\mathrm{a}}\, i_{\mathrm{b}}\, i_{\mathrm{c}}]^{\mathrm{T}}$, and $[u]_{\mathrm{abc}}$ represents the control input vector $[\sum h_{\mathrm{ia}} \sum h_{\mathrm{ib}} \sum h_{\mathrm{ic}}]^{\mathrm{T}}$($i$=1,…$N$).

Park transform is as following:

$$\boldsymbol{T}_{\mathrm{abc/dq0}} = \frac{2}{3}\begin{pmatrix} \cos\omega t & \cos(\omega t - 120°) & \cos(\omega t + 120°) \\ \sin\omega t & \sin(\omega t - 120°) & \sin(\omega t + 120°) \\ 0.5 & 0.5 & 0.5 \end{pmatrix} \tag{4}$$

Applying park transform to Equ. (3), a two-phase rotating frame d-q model of CHB is obtained as:

$$\begin{cases} \dfrac{di_{\mathrm{d}}}{dt} = -\dfrac{R_{\mathrm{s}}}{L_{\mathrm{s}}} i_{\mathrm{d}} + \omega i_{\mathrm{q}} + \dfrac{v_{\mathrm{sd}}}{L_{\mathrm{s}}} - \dfrac{v_{\mathrm{dcef}}}{L_{\mathrm{s}}} \sum_{i=1}^{N} h_{\mathrm{id}} \\ \dfrac{di_{\mathrm{q}}}{dt} = -\omega i_{\mathrm{d}} - \dfrac{R_{\mathrm{s}}}{L_{\mathrm{s}}} i_{\mathrm{q}} + \dfrac{v_{\mathrm{sq}}}{L_{\mathrm{s}}} - \dfrac{v_{\mathrm{dcef}}}{L_{\mathrm{s}}} \sum_{i=1}^{N} h_{\mathrm{iq}} \end{cases} \tag{5}$$

where v_{sd}, v_{sq}, i_{d}, i_{q}, $\sum h_{\mathrm{id}}$ and $\sum h_{\mathrm{iq}}$ are the ac voltages, grid currents, and control input signals in synchronously rotating d-q coordinates, respectively; and v_{sq}=0 under the proper synchronization of the space-vector transformation.

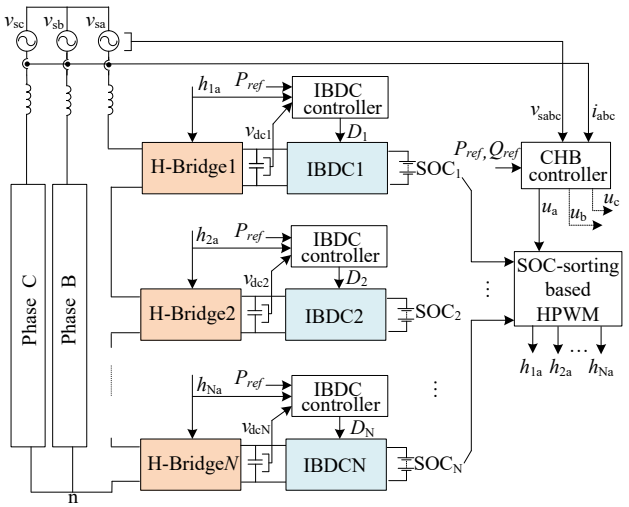

Fig. 2 Block diagram of proposed overall coordinative control strategy for PET-BESS

The dc-link voltage is determined by the difference between output dc current i_{hdi} of H-bridge rectifier and input dc current i_{Ldi} of IBDC, as is given by

$$\begin{cases} i_{\mathrm{Ldi}} = \dfrac{n_{\mathrm{t}} v_{\mathrm{bi}}}{2 f_{\mathrm{s}} L_{\mathrm{t}}} D_i (1 - |D_i|) \\ C_{\mathrm{i}} \dfrac{\mathrm{d}\, v_{\mathrm{dci}}}{\mathrm{d}\, t} = i_{\mathrm{hdi}} - i_{\mathrm{Ldi}} = h_{\mathrm{ia}} i_{\mathrm{a}} - \dfrac{n_{\mathrm{t}} v_{\mathrm{bi}}}{2 f_{\mathrm{s}} L_{\mathrm{t}}} D_i (1 - |D_i|) \end{cases} \tag{6}$$

where D_{i} and f_{s} respectively represent the phase shift ratio and switching frequency of IBDC[11]. According to (6), the dc-link voltage control can be realized by both outer loop of grid current controller of CHB and direct phase shift regulation of IBDC. Since the battery voltages change much slowly in contrast to other variables such as dc-link voltages and grid currents, the IBDC output voltage v_{bi} can be regarded as a constant and does not need to be controlled, thus the IBDC is used to regulate the dc-link in this paper by adjusting the phase shift ratio directly.

B. Overall Coordinative Control Strategy for PET-BESS

According to the above mathematic analysis, the overall coordinative control system of PET-BESS, as depicted in Fig. 2, includes three parts: 1) the total active and reactive power control for the three-phase star-configured CHB rectifier based on the state feedback method in the d-q coordinates; 2) the dc-link voltage control on IBDC by phase shift ratio with feedforward of power reference and switch status (switch functions) of CHB; 3) the HPWM multilevel modulation for CHB which aims at balancing control of the submodule battery SOC values, SOC_1~ SOC_N.

In practical applications, there are some other concerns which should be considered, such as the power limit of the battery units and power variation rate of BESS, which are determined by Battery Energy Management System (BEMS) [1] and are not discussed in this paper.

III. PRINCIPLE AND DESIGNING OF CONTROLLERS

A. State-Feedback Optimal Control for CHB Rectifier

By defining the state vector $\boldsymbol{x}=(i_{\mathrm{d}}\ i_{\mathrm{q}})^{\mathrm{T}}$ and control input vector $\boldsymbol{u}=(\sum h_{\mathrm{id}}\ \sum h_{\mathrm{iq}})^{\mathrm{T}}$, Equ. (5) can be grouped into the following MIMO affine linear form[20]:

$$\begin{cases}\dot{\boldsymbol{x}}=\boldsymbol{M}\boldsymbol{x}+\boldsymbol{b}+\boldsymbol{N}\boldsymbol{u}\\ \boldsymbol{y}=\boldsymbol{x}-\boldsymbol{d}\end{cases} \tag{7}$$

$$\mathbf{M}=\begin{pmatrix}-\dfrac{R_{\mathrm{s}}}{L_{\mathrm{s}}} & \omega\\ -\omega & -\dfrac{R_{\mathrm{s}}}{L_{\mathrm{s}}}\end{pmatrix},\ \mathbf{b}=\begin{pmatrix}+\dfrac{v_{\mathrm{sd}}}{L_{\mathrm{s}}}\\ 0\end{pmatrix},$$
$$\mathbf{N}=-\frac{v_{\mathrm{dcref}}}{L_{\mathrm{s}}}\begin{pmatrix}1 & 0\\ 0 & 1\end{pmatrix},\ \mathbf{d}=\begin{pmatrix}i_{\mathrm{dref}}\\ i_{\mathrm{qref}}\end{pmatrix} \tag{8}$$

By observing its structure, Equ. (7) can be identified as affine linear form for $\boldsymbol{N}$ is a constant matrix; M denotes the coefficient matrix, while $\boldsymbol{b}$ and $\boldsymbol{d}$ denotes the affine items.

Then the original affine control system can be easily transformed into a Brunovsky normalized linear form, as demonstrated in (9), through the state-feedback control law illustrated in (10).

$$\begin{cases}\dot{\boldsymbol{z}}=\boldsymbol{A}\boldsymbol{z}+\boldsymbol{B}\boldsymbol{v}\\ \boldsymbol{y}=\boldsymbol{z}\end{cases},\ \boldsymbol{A}=\begin{pmatrix}0 & 0\\ 0 & 0\end{pmatrix},\boldsymbol{B}=\begin{pmatrix}1 & 0\\ 0 & 1\end{pmatrix} \tag{9}$$

$$\boldsymbol{u}=-\boldsymbol{N}^{-1}(\boldsymbol{M}\boldsymbol{x}+\boldsymbol{b}-\boldsymbol{v})$$
$$=\begin{pmatrix}u_1\\ u_2\end{pmatrix}=\frac{1}{v_{\mathrm{dcref}}}\begin{pmatrix}-R_{\mathrm{s}}i_{\mathrm{d}}+L_s\omega i_{\mathrm{q}}+v_{\mathrm{sd}}-L_sv_1\\ -L_s\omega i_{\mathrm{d}}-R_{\mathrm{s}}i_{\mathrm{q}}-L_sv_2\end{pmatrix} \tag{10}$$

where $\boldsymbol{z}=\boldsymbol{x}-\boldsymbol{d}$ denotes the new state variable, and $\boldsymbol{v}=(v_1\ v_2)^{\mathrm{T}}$ denotes the new control variable vector.

Since $\boldsymbol{v}$ is the control variable of the Brunovsky normalized form, it can be determined by the LQR method [21]. Note that system (9) is easier to handle since matrix A and B are so trivial. According to LQR method, the quadratic performance index is defined in Equ. (11):

$$J=\frac{1}{2}\int_0^{\infty}(\boldsymbol{z}^T\boldsymbol{Q}\boldsymbol{z}+\boldsymbol{v}^T\boldsymbol{R}\boldsymbol{v})\,\mathrm{d}t \tag{11}$$

where $\boldsymbol{Q}$ is a positive definite (or semi-definite) symmetric matrix, and $\boldsymbol{R}$ is a positive definite symmetric matrix. The physical meanings of the performance index are explained as follows: the first item indicates that the state error is close to zero during the control process, and the second item aims to restrict the amplitude of the control variables.

Based on LQR method, the optimal control law is expressed as follows:

$$\boldsymbol{v}^*=-\boldsymbol{K}^*\boldsymbol{z}(t)=-\boldsymbol{K}^*\begin{pmatrix}i_{\mathrm{d}}-i_{\mathrm{dref}}\\ i_{\mathrm{q}}-i_{\mathrm{qref}}\end{pmatrix} \tag{12}$$

where the gain matrix is $\boldsymbol{K}^*=\boldsymbol{R}^{-1}\boldsymbol{B}^T\boldsymbol{P}$, and $\boldsymbol{P}$ is the positive definite symmetric solution of the Riccati equation $\boldsymbol{PA}+\boldsymbol{A}^{\mathrm{T}}\boldsymbol{P}-\boldsymbol{PBR}^{-1}\boldsymbol{B}^{\mathrm{T}}\boldsymbol{P}+\boldsymbol{Q}=\boldsymbol{0}$, which can be simplified to $-\boldsymbol{PR}^{-1}\boldsymbol{P}+\boldsymbol{Q}=\boldsymbol{0}$ in our case.

However, due to the dependence of the affine linear transformation on the parameters of system and converter as shown in (10), the zero steady-state error when subject to temperature or aging parameter variations cannot be ensured by using the simple proportional feedback control law of (12). To solve this problem, the integral term is introduced to the state variable vector, as given by

$$\boldsymbol{z}=\begin{pmatrix}\xi_1 & z_1 & \xi_2 & z_2\end{pmatrix}^T. \tag{13}$$

where $\xi_1=\int z_1\mathrm{d}t$, $\xi_2=\int z_2\mathrm{d}t$.

Substituting (13) in to (9) and (12) yields an expanded linear normal form of the CHB system as shown in (14), with its new feedback control law shown in (15).

$$\begin{cases}\dot{\boldsymbol{z}}=\boldsymbol{A}\boldsymbol{z}+\boldsymbol{B}\boldsymbol{v}\\ \boldsymbol{y}=\boldsymbol{z}\end{cases}$$
$$\boldsymbol{A}=\begin{pmatrix}0 & 1 & 0 & 0\\ 0 & 0 & 0 & 0\\ 0 & 0 & 0 & 1\\ 0 & 0 & 0 & 0\end{pmatrix},\ \boldsymbol{B}=\begin{pmatrix}0 & 0\\ 1 & 0\\ 0 & 0\\ 0 & 1\end{pmatrix},\boldsymbol{v}=\begin{pmatrix}v_1\\ v_2\end{pmatrix} \tag{14}$$

$$\begin{pmatrix}v_1\\ v_2\end{pmatrix}=-\boldsymbol{K}^*\begin{pmatrix}\xi_1 & z_1 & \xi_2 & z_2\end{pmatrix}^{\mathrm{T}}$$
$$=-\begin{pmatrix}k_1 & k_2 & 0 & 0\\ 0 & 0 & k_3 & k_4\end{pmatrix}\begin{pmatrix}\int(i_{\mathrm{d}}-i_{\mathrm{dref}})dt\\ i_{\mathrm{d}}-i_{\mathrm{dref}}\\ \int(i_q-i_{\mathrm{qref}})dt\\ i_q-i_{\mathrm{qref}}\end{pmatrix} \tag{15}$$

With the integral term added to the linear feedback control law as shown in (15), the zero steady-state error and robustness of CHB controller can be enhanced.

To solve the feedback gain matrix K^* through the LQR method, the weight matrix $\boldsymbol{Q}$ and $\boldsymbol{R}$ of the quadratic performance index shown in (11) must be determined first. For matrix $\boldsymbol{Q}$, the system energy function is constructed as:

$$H=\boldsymbol{z}^T\boldsymbol{Q}\boldsymbol{z}=\frac{L_s}{2}(\xi_1^2+z_1^2+\xi_2^2+z_2^2) \tag{16}$$

By substituting $\boldsymbol{z}=(\xi_1\ z_1\ \xi_2\ z_1)^T$ into (16), matrix $\boldsymbol{Q}$ can be determined as

$$\boldsymbol{Q}=\frac{L_s}{2}\begin{pmatrix}1 & 0 & 0 & 0\\ 0 & 1 & 0 & 0\\ 0 & 0 & 1 & 0\\ 0 & 0 & 0 & 1\end{pmatrix} \tag{17}$$

And another weighted matrix $\boldsymbol{R}$ is selected as

$$\boldsymbol{R}=\frac{L_s^2}{f_{\mathrm{c}}}\begin{pmatrix}1 & 0\\ 0 & 1\end{pmatrix} \tag{18}$$

where f_{c} is the equivalent switching frequency of CHB rectifier. It can be seen that $\boldsymbol{Q}$ is indeed positive demi-definite and $\boldsymbol{R}$ is indeed positive definite.

Then substituting $\boldsymbol{A}$, $\boldsymbol{B}$, $\boldsymbol{Q}$ and $\boldsymbol{R}$ shown in (14), (17) and (18) into the Riccati equation, matrix $\boldsymbol{P}$ and matrix $\boldsymbol{K}^*$ can be

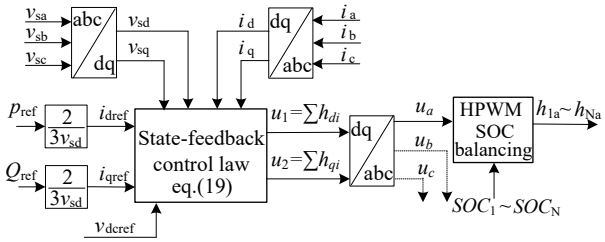

Fig. 3 Block diagram of CHB control

determined. Substituting matrix $\boldsymbol{K}^*$ into (15) and (10) yields the control vector $\boldsymbol{u}$ for the original system shown as follows

$$\begin{cases} u_1 = \dfrac{L_s\omega i_q - R_s i_d + v_{sd} + L_s(k_1\xi_1 + k_2 z_1)}{v_{dcref}} \\ u_2 = \dfrac{-L_s\omega i_d - R_s i_q + L_s(k_3\xi_2 + k_4 z_2)}{v_{dcref}} \end{cases} \tag{19}$$

Based on (19), the control block diagram of CHB rectifier is shown in Fig. 3, where u_a, u_b, and u_c are the modulating signals in three-phase frame obtained by the inverse park transform of u_1, u_2. And by using HPWM SOC-balancing strategy, the switching functions of each H-bridge rectifier can be obtained. The current commands in the *d*-axis and *q*-axis, i_{dref} and i_{qref}, are calculated from the active and reactive power commands, p_{ref} and q_{ref} [3], as given by

$$i_{dref} = 2P_{ref}/(3v_{sd}),\ i_{qref} = 2Q_{ref}/(3v_{sd}) \tag{20}$$

It should be noted that the designed optimal controller in the *d-q* coordinates can also be applied to the single-phase CHB system by utilizing the single-phase d-q transformation, in which an imaginary phase M, lagging 90˚ from the real phase A, must be hypothesized [16].

B. DC-Link Voltage Controller for IBDC

A set of stable and balanced dc-link voltages is prerequisite for stable operation as well as the high quality output ac waveforms of PET-BESS, especially under bidirectional changed power flow and uneven SOC of the submodule battery units. In this subsection, the control design of the dc-link voltages for IBDC is conducted.

According to Equ. (6), the dependence of the dc-link voltage on the phase shift ratio of IBDC can be illustrated as a first order differential equation. Conventional control schemes of IBDC can be classified into two types: single loop voltage control [22] and voltage current double loop control [23]. Fig. 4(a) shows the diagram of IBDC under voltage control, which is current sensorless. However, the power reference of CHB varies frequently due to the application of BESS, and it will interfere in the stability control of dc-link. The illustration mentioned above is described as an interference path in Fig. 4(a), in which G_{CHB} is the transfer function from the active current reference i_{dref} to the dc-link input current i_{hdi}.

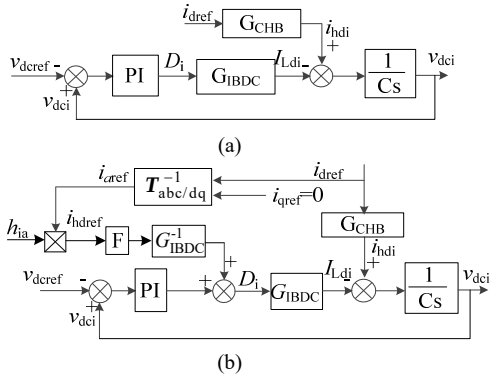

Fig. 4 Control diagram for IBDC. (a) Conventional one-loop control. (b) Coordinative control with feedforward loop.

In order to reduce the interference of the power reference on the dc-link voltage, a coordinative control strategy with participation of the CHB signals is presented, as shown in Fig. 4(b), where the active current reference and switch status of CHB form a feed-forward path to the dc-link voltage control.

In Fig. 4(b), i_{aref} denotes the sinusoidal current reference of CHB in phase A, which can be obtained through the inverse park transform, $\boldsymbol{T}^{-1}_{abc/dq}$, of i_{dref} and i_{qref}. G_{IBDC} is the transfer function from the phase shift ratio D_i to input dc current i_{Ldi} of IBDC, which can determined according to (6).

$$G_{IBDC} = \frac{i_{Ldi}}{D_i} = \frac{n_t v_{bi}}{2 f_s L_t}(1 - 2|\overline{D_i}|) \tag{21}$$

where $\overline{D_i}$ is the mean value of the phase shift ratio.

Being directly added to the phase shift ratio, as shown in Fig. 4(b), the feed-forward path will introduce high frequency ripples to the dc-link voltage control. To avoid this disadvantage, a second-order low pass filter F is added into the feed-forward path to compensate for the high frequency component, with its transfer function shown as follows:

$$F(s) = \frac{\omega_n^2}{s^2 + 2\xi\omega_n s + \omega_n^2} \tag{22}$$

Where ω_n and ξ are the natural frequency and damping ratio of the filter respectively.

According to Fig. 4(a), the dc-link voltage PI controller can be designed by its compensated open loop transfer function, as expressed in (23).

$$G(s) = (k_{vp} + \frac{k_{vi}}{s})\frac{G_{IBDC}}{Cs}\frac{1}{Ts+1} \tag{23}$$

Where, k_{vp} and k_{vi} are the proportion and integration constants of the voltage PI controller, and a low-pass function with time constant T is added to represent the response delay of the dc current i_{Ldi}. The Bode diagram of (23) is shown in Fig. 5 with parameters given in the simulation section. As shown in Fig. 5, the phase angle with the logarithmic magnitude of 0 dB is equal to -120.9˚. Thus, the phase margin is ϕ_{pm}=180˚-120.9˚=59.1˚. The logarithmic magnitude with the phase angle of -180˚ is negative infinity; therefore the gain

margin is infinity. And the damping ratio ξ_1 can be furtherly estimated as $\xi_1 \approx 0.01\times\phi_{pm} = 0.59$ [24].

In the following, the damping effect on the dc-link voltage fluctuations of conventional and the coordinative IBDC controller is analyzed. According to Fig. 4(a) and Fig. 4(b), the interference transfer functions of conventional control and coordinative control with the input of i_{dref} and output of dc-link voltage, can be derived as in (24) and (25).

$$G_{conv} = \frac{v_{dci}}{i_{dref}} = \frac{G_{CHB}(s)}{Cs + ((k_{vp} + k_{vi}/s))G_{IBDC}} \tag{24}$$

$$G_{coor} = \frac{v_{dci}}{i_{dref}} = \frac{G_{CHB}(s) - \dfrac{v_{sd}}{2Nv_{dc}}F(s)}{Cs + ((k_{vp} + k_{vi}/s))G_{IBDC}} \tag{25}$$

It should be noted that during the derivation of (25), the input-output power balance equation of H-bridge rectifier is used, as shown in (26), where P_{aref} represents the power reference of CHB rectifier in phase A, and the N H-bridges are assumed to be power balanced.

$$P_{aref} = \frac{i_{dref}v_{sd}}{2} = Ni_{hdref}v_{dc} = Nh_{ia}i_{aref}v_{dc} \tag{26}$$

where v_{dc} is the average value of dc-link voltages. The transfer function $G_{CHB}(s)$ in the interference path is determined by the grid current controller of CHB. According to the grid current dynamic equation shown in (5) and the state-feedback control law shown in (19), the closed-loop transfer function of the active current of CHB is obtained as

$$\frac{i_d}{i_{dref}} = \frac{k_2 s + k_1}{s^2 + k_2 s + k_1} \tag{27}$$

Then the transfer function $G_{CHB}(s)$ can be expressed as

$$G_{CHB}(s) = \frac{i_{hdi}}{i_{dref}} = \frac{i_{hdi}}{i_d}\frac{i_d}{i_{dref}} = \frac{1}{2}\frac{v_{sd}}{Nv_{dc}}\frac{k_2 s + k_1}{s^2 + k_2 s + k_1} \tag{28}$$

By substituting (21), (22), (28) in to (24) and (25), the Bode plots of the interference transfer function of the two compared control methods for IBDC are depicted in Fig. 6. The parameters are given in the simulation section. As shown in Fig. 6, the interference gain of the proposed coordinative control is much smaller than that of conventional control, which indicates that under the same power reference variations, the coordinative control can maintain voltages on the dc-link with smaller fluctuations.

IV. HPWM Based SOC Balancing Strategy

Considering of the manufacturing tolerances and unequal converter cell losses, etc., the SOC imbalance problem among submodules cannot be neglected although the battey voltages do not need to be controled. In this paper, the SOC balancing function is assigned to the front CHB by incorporating the battery SOC information into the HPWM modulation algorithm of CHB.

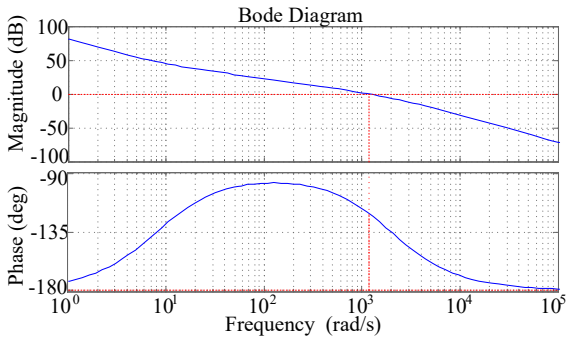

Fig. 5 Bode plots of IBDC converter under voltage control

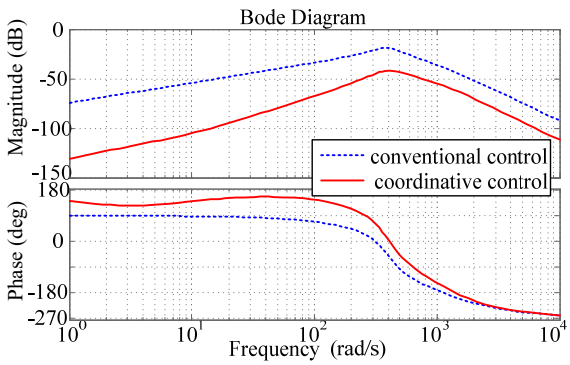

Fig. 6 Comparison of interference Bode plots between coordinative control and conventional control

The original study of the HPWM method for CHB rectifier was done by M. Moosavi, H. Iman-Eini et al. in [25], aiming at balancing the dc-link voltages and obtaining reduced switching losses and low THD as well. In this paper, the HPWM method is utilized to adjust the battery SOC to converge, in addition to the merits of reduced switching frequency and low THD.

Principle of the HPWM-based SOC-balancing method is illustrated in Fig. 7, where h_1~h_N are the switch functions for each H-bridge in a sequence with the corresponding battery SOC values arranged in an ascending order. According to Fig. 7, when u_a>0 and i_a>0, the battery units with lower SOC will be charged as the corresponding switch functions equal 1 (or a charging PWM), while the ones with higher SOC will be discharged as the corresponding switch functions equal -1 (or a discharging PWM). Actrully, for each H-bridge unit, when i_a>0, h_i=1 means positive output voltage and charging power into the battery unit; while h_i=-1 means negative voltage and discharge process. On the contrary, when i_a<0, h_i=1 means discharging while h_i=-1 means charging. It is the different power flow among submodules that drives the SOC of all battery units to converge and balance at last.

Therefore, according to Fig. 7, the flowchart of the rules based on the voltage region variable k and SOC sorting of battery-units are presented in Fig. 8 to carry out the switch functions of each H-bridge [25].

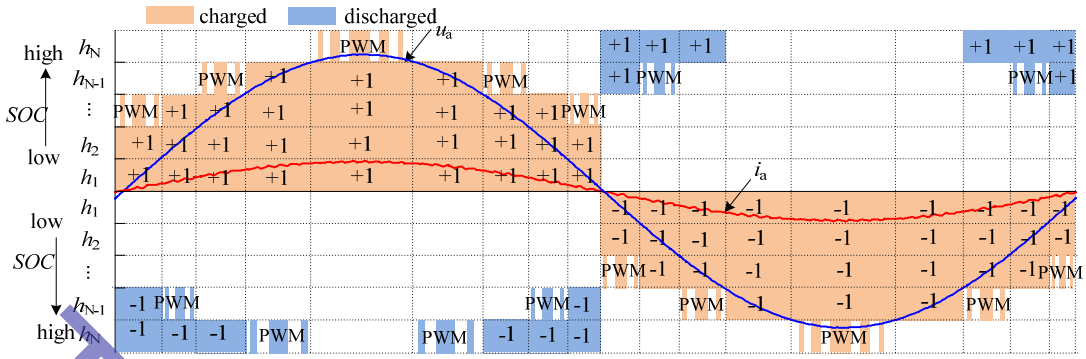

Fig. 7 Principle of HPWM modulating strategy based on SOC sorting

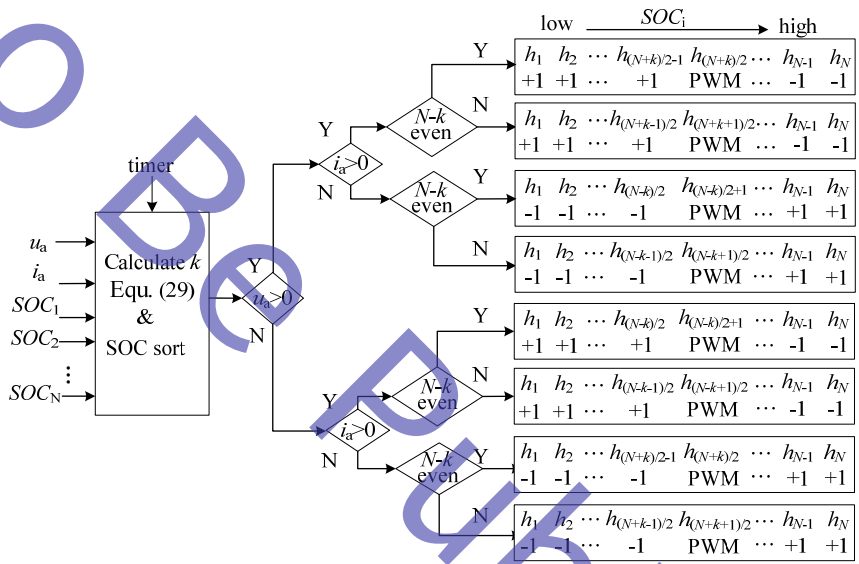

Fig. 8 Flowchart of HPWM-SOC balancing algorithm

The voltage region k is defined as follows:

$$k = \text{floor}(|u_a|) + 1, \quad k = 1, 2, \ldots N \tag{29}$$

where the function floor(·) represents the rounding calculation to the nearest integer towards zero.

And the modulating signal of the H bridge that works in PWM mode is calculated as

$$u_t = u_a - (k-1)\,\text{sign}(u_a) \tag{30}$$

V. Simulation and Experimental Verification

A. Simulation Results

A simulation model based on Fig. 1 has been built in MATLAB/Simulink to validate the proposed control strategy. The PET-BESS model consists of five H-bridge-IBDC units per phase, with each unit rated power of 166 kW (240kW peak), total power of 2.5 MW, and line-to-neutral voltage of 10 kV^{rms}. This configuration can be easily extended to the medium voltage system with the ratings of 35 kV (line-to-line) and 5MW, which is usually used for integrating the megawatt-scale PV or wind power plants [6]. All the parameters of the system and circuits are listed in Table I. It should be noted that the small capacity battery models of 300V/28A·h (not realistic) are chosen for simulation in this paper to obtain an observable charge or discharge process in a short simulation time, while in practical, battery pack with large capacity should be utilized (e.g., 300V, 2000Ah).

By using MATLAB instruction $\boldsymbol{K}$=lqr($\boldsymbol{A}$, $\boldsymbol{B}$, $\boldsymbol{Q}$, $\boldsymbol{R}$), the feedback gains for CHB controller can be obtained as k_1=559, k_2=560, k_3=559 and k_4=560. With these control parameters, the bandwidth of CHB current controller is about 800 rad/s. The second-order filter F in the feed-forward path is chosen to have the same bandwidth as that of CHB. Under this condition, the natural frequency and damping ratio of the filter can be set as ω_n=1200, ξ=1. The proportion and integration constants of the IBDC PI controller are k_{vp}=0.0081 and k_{vi}=0.0652, respectively.

The simulation condition is given as follows: the bidirectional active power reference P_{ref} varies between 2.5MW and -2.5MW with the period of 0.8s, while Q_{ref} is set as 0VA for unity power factor. The initial battery-unit SOC

TABLE I. Simulation Parameters for PET-BESS

Parameter	Symbol	Value
Line-to-neutral rms voltage	v_{sabc}	10 kV
Total power rating	P_{ref}	2.5 MW
Nominal dc-link voltage	v_{dcref}	3000 V
Input filter inductance	L_s	8 mH
Dc-link capacitor	C_i	20 mF
Leakage inductance of IBDC	L_t	0.152mH
Turn ratio of HF transformer	n_t	10
CHB' PWM carrier frequency	f_c	2 kHz
Switching frequency of IBDC	f_s	5 kHz
Battery nominal voltage		300 V
Battery nominal capacity		28 Ah

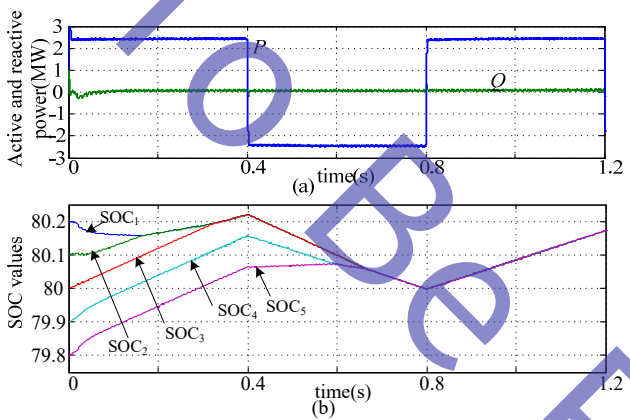

Fig. 9 Simulation waveforms of (a) three-phase active power P and reactive power Q (b) SOC curves of submodule battery units in phase A

are set as 80.2%, 80.1%, 80%, 79.9% and 79.8% respectively to validate the HPWM based SOC balancing strategy.

Simulation waveforms of the three-phase active and reactive power as well as the submodule battery SOC curves in phase A are demonstrated in Fig. 9. The results confirm that the active and reactive power track the power commands well with high dynamic performance, and during the charge and discharge processes, the submodule battery SOC values converge effectively.

Fig. 10 shows the compared dc-link voltage responses between the proposed coordinative control and the conventional control for IBDC. As can be seen, when power reversed at 0.4s and 0.8s, there are significant drops and rises on the dc-link voltages under the conventional control, while under the proposed control the voltage drops and rises are much smaller.

Fig. 11 (a) shows the three-phase eleven-level ac output voltages of CHB, which do not change obviously at 0.4s when the active power reversed, due to high control performance of the dc-link voltages. The three-phase voltages and currents of the grid are shown in Fig.11 (b), which are in phase before 0.4s and out of phase after 0.4s under the condition of Q_{ref}=0. And the dynamic process of grid current

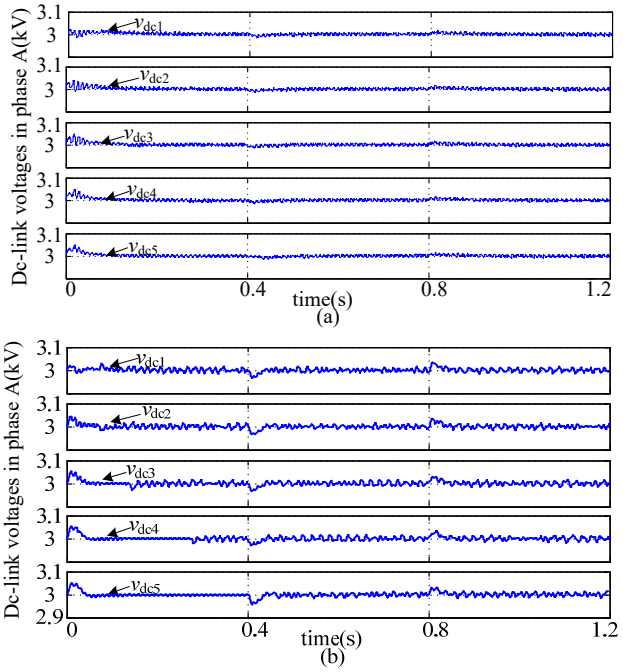

Fig. 10 Waveform comparison of dc-link voltages in phase A, v_{dc1}-v_{dc5}, under (a) proposed coordinative control for IBDC, (b) conventional control for IBDC

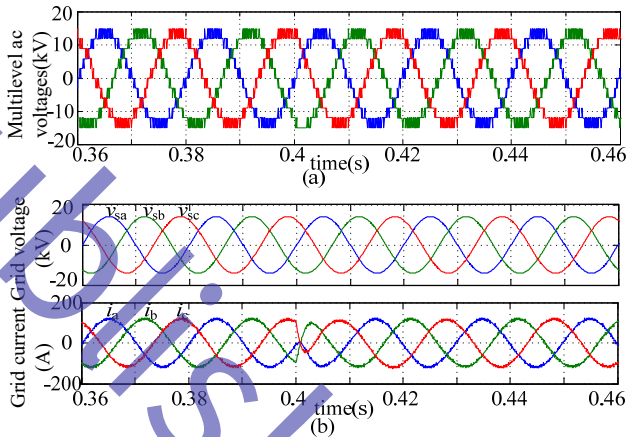

Fig. 11 Detailed waveforms of (a) three-phase multilevel ac voltages (b) three-phase grid voltages and grid currents.

takes less than one line cycle, which demonstrates a good performance of the proposed state-feedback CHB controller.

B. Experimental Results

The proposed control method is validated on a laboratory scale prototype with one phase leg, as shown in Fig. 12. The prototype consists of one main controller unit (MCU), a CHB converter and five IBDC. The grid voltage is 200V^{rms} (50 Hz); the rated power is 2kW, and the utilized battery cells are of Valve Regulated Lead Acid (VRLA) 60V/28A·h technology; the dc-link capacitors are 4700 μF, and the dc-link voltage reference is 60V, the turn ratio of the IBDC HF transformer is 1:1. Other parameters are the same with those in Table I.

In MCU and each submodule, a TMS320F28335 DSP is applied for the validation of the proposed control algorithm, and a Xilinx XC3S400 FPGA chip is responsible for

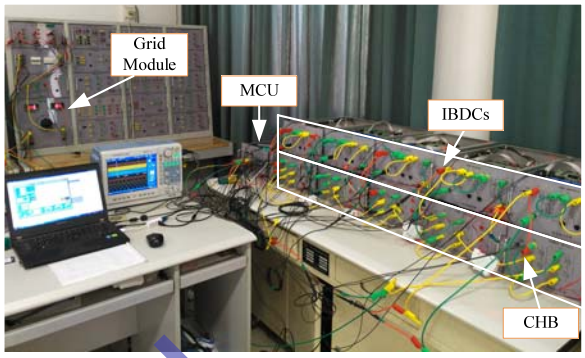

Fig. 12 Experimental setup of single phase PET-BESS

processing the communication task and/or generating the firing pulses. All the control signals are transmitted via optical fibers between MCU and CHB or IBDC submodules. As is mentioned in section 4, the SOC sorting for the multiple battery units is used in the HPWM method. Unfortunately, for the absence of the battery energy management system (BEMS) in the lab at present, the SOC values are not available. As an alternative, to validate the HPWM based battery balancing strategy, the sorting of terminal voltages of the batteries is used to approximate the sorting of SOC.

Firstly, experiment waveforms of the PET-BESS, including the dc-link and battery voltage v_{dc1} and v_{b1}, grid voltage v_{sa}, grid current i_a, and synthesized multilevel ac voltage v_{an} (defined in Equ. (1)), are provided in Fig. 13(a). Corresponding results of the single-stage CHB-BESS are also given for comparison, which is shown in Fig. 13(b). During the experiment, the active power command P_{ref} is step changed from 800W to -800W.

As can be seen, in the PET-BESS, the dc-link voltage v_{dc1} can be effectively controlled to be constant when the active power reversed and the battery terminal voltage v_{b1} dropped. The steady state waveform of i_a is sinusoidal and undistorted, and the multilevel ac voltage v_{an} is of good quality. Due to the well-designed CHB controller, the dynamic process of grid current takes less than 0.02s. However, in the single-stage CHB-BESS, the dc-link voltage (equals to the battery voltage) drops about 5V (8.3%) after power reversion due to the internal resistance of battery. The voltage drop leads to the over-modulation of CHB, which causes distortions of steady state waveforms of v_{an} and i_a.

Fig. 14 gives the ac terminal voltages of each H-bridge rectifier and the synthesized eleven-level voltage, under the condition of a positive active power. As is observed, the first, third and fifth H-bridge operate in the charge mode, for there are only unipolar switching modes in half grid cycle for the three H-bridges; while there are both positive and negative (combining with PWM) switching modes in half grid cycle for the second and fourth H-bridge, which work alternately in charge and discharge process as a result. The results are in accordance with the HPWM algorithm in Section 4.

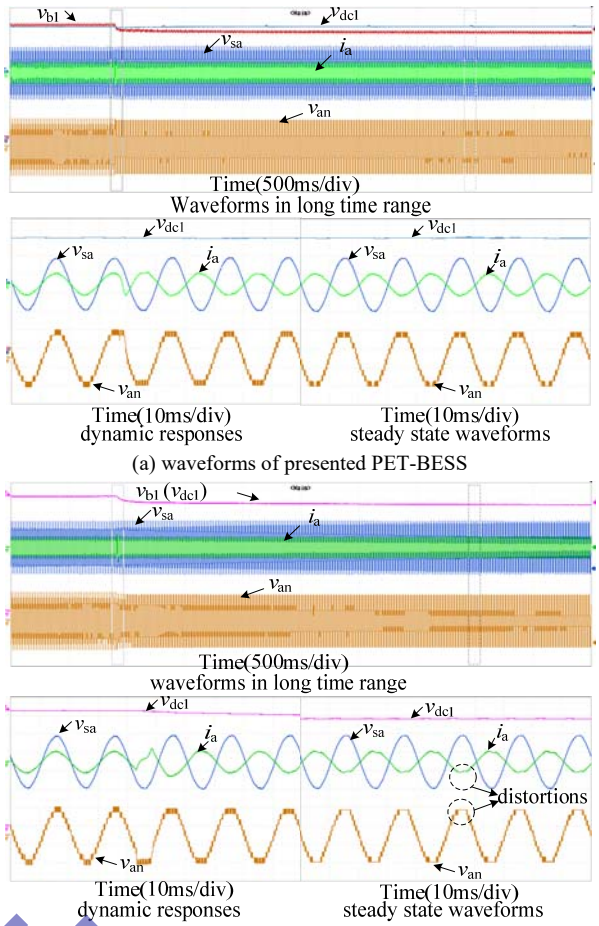

Fig. 13 Comparison waveforms of BESS with and without IBDC, including grid voltage and multilevel ac voltage, v_{sa} and v_{an} (200V/div), grid current i_a (10A/div), dc-link and battery voltage v_{dc1} and v_{b1} (10V/div)

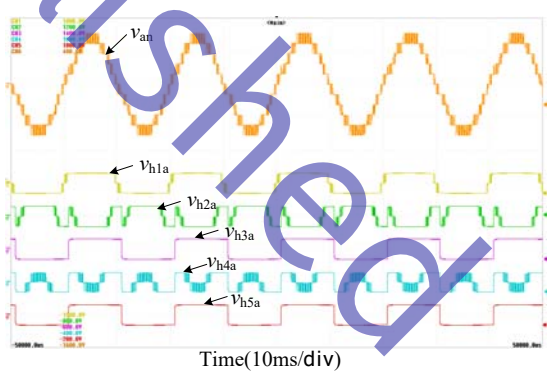

Fig. 14 AC terminal voltage of each H-bridge, v_{h1a}~v_{h5a} (200V/div), and synthesized multilevel ac voltage v_{an} (200V/div)

Fig. 15 shows the compared dc-link voltage responses between the proposed coordinative control and conventional control for IBDC, to a step change of the active power reference (800W to -800W). As can be seen, the dc-link voltage drops are much smaller when the coordinative scheme is used, and the dynamic process is faster.

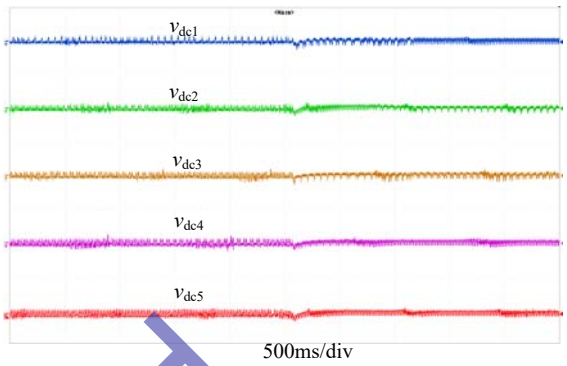

(a) dc-link voltages under coordinative IBDC controller

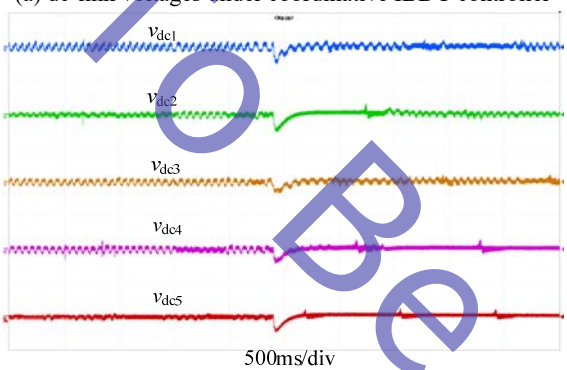

(b) dc-link voltages under conventional IBDC controller

Fig. 15 Dc-link voltages v_{dc1}-v_{dc5} (2V/div) with a 60V dc bias under two control strategies for IBDC

Fig. 16 shows the voltage and current waveforms of IBDC in the bidirectional power flow cases. v_{dc1} and v_{b1} are the dc-link and battery terminal voltages. v_{pri} and v_{sec} are ac voltages on the primary side and secondary side of the transformer. i_{L1} is the inductive current. As is shown, with IBDC controlling, the dc-link voltage can maintain a constant value of 60V, when the power reversed and a voltage drop appeared on the battery terminal voltage. In the charge mode, the square wave voltage of primary side leads the square wave voltage of secondary side by a small phase angle; while in the discharge mode, the results are opposite. These results indicate that the IBDC circuits operate correctly.

Fig. 17 provides the five convergent battery-unit terminal voltages, during long-time charge and discharge process. The results confirm the validity of the HPWM-based battery balancing method. It should be noted that due to the internal impedance of the battery units, a voltage drop appears in all the battery voltages when the power flow reversed.

VI. Conclusions

This paper presents a coordinative control strategy for PET-BESS, which is based on the topology of CHB and IBDC. In the proposed method, the functions of power control and battery SOC balancing are assigned to the front CHB, while the dc-link voltages are controlled by the IBDC,

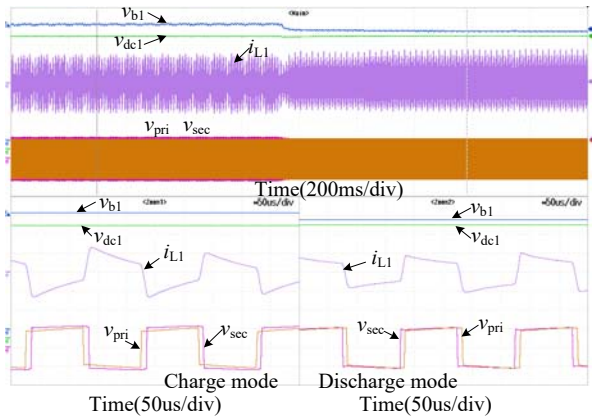

Fig. 16 Waveforms of IBDC variables, including the input and output dc voltages of IBDC, v_{dc1} and v_{b1} (10V/div), inductive ac current i_{L1} (5A/div), and primary and secondary side ac voltages, v_{pri} and v_{sec} (50V/div)

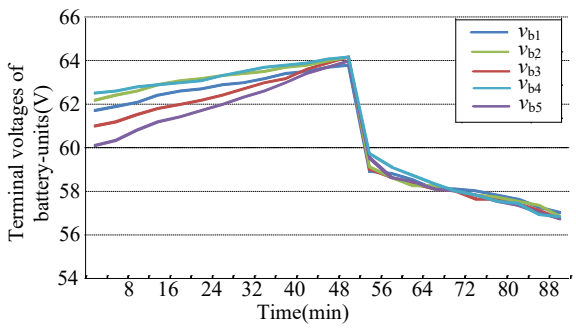

Fig. 17 Variation in terminal voltages of the five battery-units

with the power reference and switch status of CHB taken as a feedforward. Better dynamic performances of ac current, active and reactive power can be achieved by state feedback and LQR methods for CHB under bidirectional power flow. The feedforward of power reference and switch status of CHB effectively reduces the dc-link voltage fluctuations under power variations. With the battery SOC information incorporated into the HPWM modulation of CHB, the SOC curves of submodule battery-units converge effectively. Finally, simulations on the three-phase PET-BESS model and experiments on a single-phase scale-down prototype are conducted to confirm effectiveness of the presented control method.

Acknowledgment

This work was supported by the Fundamental Research Funds for the Central Universities under Grand No. 2017MS099, and the Independent Research Project of State Key Laboratory of Alternate Electrical Power System with Renewable Energy Sources (North China Electric Power University) under Grand No. LAPS2016-08.

REFERENCES

[1] M. Sedghi, A. Ahmadian, E. Pashajavid, et al, "Storage scheduling for optimal energy management in active distribution network considering load, wind, and plug-in electric vehicles uncertainties," *J. Renewable Sustainable Energy*, Vol. 7, 033120, June 2015.

[2] M. S. Ballal, K. V. Bhadane, R. M. Moharil, et al, "A control and protection model for the distributed generation and energy storage system in microgrids," *J. Power Electronics,* Vol. 16, No. 2, pp. 748-759, Mar. 2016.

[3] L. Maharjan, T. Yamagishi, and H. Akagi, "Active-power control of individual converter cells for a battery energy storage system based on a multilevel cascade PWM converter," *IEEE Trans. Power Electron.*, Vol. 27, No. 3, pp. 1099-1107, Mar. 2012.

[4] W. Wang, F. Wu, K. Zhao, et al, "Elimination of the state-of-charge errors for distributed battery energy storage devices in islanded droop-controlled microgrids," *J. Power Electronics*, Vol. 15, No. 4, pp. 1105-1118, July 2015.

[5] K. F. Krommydas, A. T. Alexandridis, "Modular control design and stability analysis of isolated PV-source/battery-storage distributed generation systems," *IEEE Journal on Emerging and Selected Topics in Circuits and Systems*, Vol. 5, No. 3, pp. 372-382, Aug./Sept. 2015.

[6] Xibo Yuan, "A set of multilevel modular medium-voltage high power converters for 10-MW wind turbines," *IEEE Trans. Sustainable Energy*, Vol. 5, No. 2, pp. 524-534, April 2014.

[7] Y. Zhuang, C. Wang, C. Wang, et al, "Determination method for topology configuration of hybrid cascaded H-bridge rectifiers," *J. Power Electronics,* Vol. 16, No. 5, pp. 1763-1772, Sep. 2016.

[8] L. Maharjan, S. Inoue, and H. Akagi, "A transformerless energy storage system based on a cascade multilevel PWM converter with star configuration," *IEEE Trans. Ind. Appl.*, Vol. 44, No. 5, pp. 1621-1630, Sep./Oct. 2008.

[9] D.-H. Shin, J.-B. Jeong, T.-H. Kim, et al, "Modeling of lithium battery cells for plug-in hybrid vehicles," *J. Power Electronics,* Vol. 13, No. 3, pp. 429-436, May 2013.

[10] I. Trintis, S. Munk-Nielsen, R. Teodorescu, "Cascaded H-bridge with bidirectional boost converters for energy storage," in *Proceedings of the 2011 European Conference on Power Electronics and Applications (EPE)*, pp. 1-9, Aug. 2011.

[11] H. Qin, Jonathan W. Kimball, "Generalized average modeling of dual active bridge dc-dc converter," *IEEE Trans. Power Electronics*, vol. 27, no. 4, pp. 2078-2084, April 2012.

[12] J. W. Kolar, G. Ortiz, "Solid-state-transformers: key components of future traction and smart grid systems," in *Proceedings of the International Power Electronics Conference-ECCE Asia (IPEC 2014)*, May 2014.

[13] B. Zhao, Q. Song, W. Liu, et al, "Overview of dual-active bridge isolated bidirectional DC-DC converter for high-frequency-link power-conversion system," *IEEE Trans. Power Electron.*, Vol. 29, No. 8, pp. 4091-4106, Aug. 2014.

[14] Z. Gao, and H. Fan, "A modular bi-directional power electronic transformer," *J. Power Electronics*, Vol. 16, No. 2, pp. 399-413, Mar. 2016.

[15] H. Iman-Eini, J-L. Schanen, Sh. Farhangi, et al, "A power electronic based transformer for feeding sensitive loads," in *Proceedings of the 2008 IEEE Power Electronics Specialists Conference*, pp. 2549-2555, Jun 2008.

[16] J. Shi, W. Gou, H. Yuan, T. Zhao, and Alex Q. Huang, "Research on voltage and power balance control for cascaded modular solid-stated transformer," *IEEE Trans. Power Electron.*, Vol. 26**,** No. 4, pp. 1154-1166, Apr. 2011.

[17] T. Zhao, G. Wang, S. Bhattacharya, and Alex Q. Huang, "Voltage and power balance control for a cascaded H-bridge converter-based solid-state transformer," *IEEE Trans. Power Electron.*, Vol. 28, No. 4, pp. 1523-1532, Apr. 2013.

[18] B. Zhao, Q. Song, W. Liu, Y. Sun, "A synthetic discrete design methodology of high-frequency isolated bidirectional DC/DC converter for grid-connected battery energy storage system using advanced components," *IEEE Trans. Ind. Electron.*, Vol. 61, No. 10, pp. 5402-5410, Oct. 2014.

[19] Q. Miao, J. Wu, H. Ai, et al, "Study on coordinating control strategy of hybrid cascade energy storage and bi-directional power regulation device," *Advanced Materials Research*, Vol. 852, pp. 655-659, Jan. 2014

[20] M. Ornik, M. E. Broucke, "A topological obstruction to reach control by continuous state feedback," in *IEEE Annual Conference on Decision and Control (CDC)*, pp. 2258-2263, Dec. 2015.

[21] D. Shuai, Y. Xie, X. Wang, "Optimal control of buck converter by state feedback linearization," in *Proceedings of the 7th World Congress on Intelligent Control and Automation*, pp. 2265-2270, June 2008.

[22] D. Segaran, D. G. Holmes, "Enhanced load step response for a bidirectional DC-DC converter," *IEEE Transactions on Power Electronics*, Vol. 28, No. 1, pp. 371-379, Jan. 2013.

[23] Y. Tian, Z. Chen, F. Deng, et al, "Active power and DC voltage coordinative control for cascaded DC-AC converter with bidirectional power application ," *IEEE Trans. Power Electron.*, Vol. 30, No. 10, pp. 5911-5925, Oct. 2015.

[24] R. C. Dorf, R. H. Bishop, *Modern Control Systems*. 12th ed., Pearson Education Group, Chapter 9, pp. 653-660, 2013.

[25] M. Moosavi, G. Farivar, H. Iman-Eini, et al, "A voltage balancing strategy with extended operating region for cascaded H-bridge converters," *IEEE Trans. Power Electron.*, Vol. 29, No. 9, pp. 5044-5053, Sep. 2014.

Yuwei Sun was born in Tangshan, China in 1987. She received her M.S. degree in Power Electronics from North China Electric Power University, Baoding, China, in 2013. She is currently working toward the Ph. D. degree in electrical engineering from North China Electric Power University, Beijing, China.

Her research interests are power electronics technology application in power system, and power electronic transformer.

Jiaomin Liu received the B.S. degree in automation from Hebei University of Technology, in 1982, and the Ph.D. degree from Hebei University of Technology in 1998. He is currently a Professor with the School of Electrical and Electronics Engineering at North China Electric Power University.

His research interests are new energy power system characteristics and multi-power sources supplementary.

Yonggang Li received the M.S. and Ph.D. degrees in electrical engineering from North China Electric Power University, in 1995 and 1999. He is currently a Professor with the School of Electrical and Electronics Engineering at North China Electric Power University.

His research interests are power system operation analysis, including renewable energy and electric equipment.

Chao Fu received the M.S. and Ph.D. degrees in electrical engineering from North China Electric Power University, in 2006 and 2012. He is currently a Lecturer with the School of Electrical and Electronics Engineering at North China Electric Power University, Baoding, China.

His research interests are renewable energy generation and power electronics technology application in power system.

Yi Wang received the B.S. and Ph.D. degrees in electrical engineering from North China Electric Power University, Beijing, China, in 1999 and 2005, respectively. He is currently a Professor with the School of Electrical and Electronics Engineering at North China Electric Power University.

His research interests include power electronics applications in power system, including wind power integration, VSC-HVDC, and dc grid.